International Journal of Multiphase Flow 196 (2026) 105558

Contents lists available at ScienceDirect

International Journal of Multiphase Flow

journal homepage: www.elsevier.com/locate/ijmulflow

Research paper

# A weakly-compressible DEM–CFD framework for dense gas–solid multiphase flows: Foundations consistent with reactive coupling

Yuki Yakata [a], Kimiaki Washino [a], Masaya Muto [b], Ryoichi Kurose [c], Takuya Tsuji [a,*]

[a] Department of Mechanical Engineering, The University of Osaka, 2-1 Yamada-oka, Suita, 565-0871, Osaka, Japan
[b] Department of Environmental Science and Technology, Meijo University, 1-501 Shiogamaguchi, Tempaku-ku, 468–8502, Nagoya, Japan
[c] Department of Mechanical Engineering and Science, Kyoto University, Kyoto daigaku-Katsura, Nishikyo-ku, 615-8540, Kyoto, Japan

## GRAPHICAL ABSTRACT

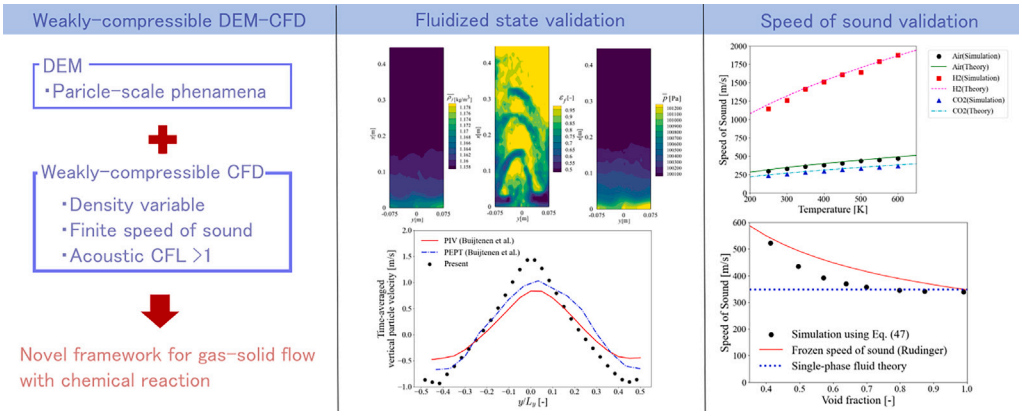


## HIGHLIGHTS

- A new DEM–CFD framework for low-Mach number flows is developed based on weakly-compressible formulation.
- The proposed framework efficiently captures both particle-scale physics and acoustic phenomena.
- Gas–particle momentum exchange is validated via pressure drop tests against the Ergun equation.
- Fluidized bed simulations reproduce experimental dynamics and high sensitivity to DEM parameters.
- The framework accurately predicts the speed of sound in various gases within a particle bed.

## ARTICLE INFO

*Keywords:*
DEM–CFD
Fluidized bed
Weakly-compressibility
Fractional-step method
Chemical reactions
Speed of sound

## ABSTRACT

The design of large-scale multiphase reactors, such as fluidized beds for methanation, requires numerical methods that are both computationally efficient and physically accurate. This study addresses the limitations of existing approaches, where traditional DEM–CFD solvers are often computationally expensive and computationally less expensive methods typically fail to capture crucial physical phenomena such as finite-speed acoustic waves. We present a novel DEM–CFD framework for low-Mach number flows that couples the Discrete Element Method (DEM) with a non-iterative, weakly-compressible fractional-step method for the gas phase. This approach combines the particle-scale accuracy of DEM with a gas solver that efficiently handles both density variations and acoustic wave propagation. As a fundamental step before simulating

* Corresponding author.
*E-mail address:* tak@mech.eng.osaka-u.ac.jp (T. Tsuji).

https://doi.org/10.1016/j.ijmultiphaseflow.2025.105558
Received 26 September 2025; Received in revised form 11 November 2025; Accepted 23 November 2025
Available online 27 November 2025

reactive flows, this paper validates the framework's hydrodynamic and acoustic capabilities using non-reactive test cases. First, simulations of pressure drop across a fixed bed show excellent agreement with the Ergun equation, validating the momentum exchange model. Second, the complex dynamics of a spout-fluidized bed are shown to reproduce experimental trends, while also highlighting the simulation's sensitivity to particle contact parameters like restitution and friction coefficients. Finally, speed of sound measurements in various gases (Dry Air, $CO_2$, $H_2$) within a particle bed confirm the framework's ability to accurately capture finite sound speed and species-dependent properties, with results aligning well with pure-gas theory. The framework's flexibility was further demonstrated by successfully reproducing an alternative "frozen" two-phase sound speed. These comprehensive validations demonstrate the framework's capability as a robust and efficient tool for investigating complex reactive multiphase flows.

## 1. Introduction

Dense gas–solid multiphase flows with chemical reaction are prevalent in a wide range of industrial applications, making a thorough understanding of their behavior crucial for process optimization and safety. A typical example is the use of fluidized bed reactors for methanation, a catalytic process that converts $CO_2$ or CO and $H_2$ into $CH_4$ and $H_2O$ that is gaining attention as a key technology for achieving carbon neutrality. Fluidized beds are particularly effective for such processes due to their excellent mixing properties and uniform temperature distribution, which are advantageous for large-scale, efficient operation. However, significant challenges arise from the chemical reaction and associated gas density changes. As reported by Kai et al. (2006), reactions such as methanation that involve a net decrease in the number of gas moles can alter the gas density, which in turn can degrade fluidization quality. Furthermore, recent study indicates that gas compressibility can become significant even well below the Mach number threshold of 0.3. This occurs particularly in systems dominated by heat exchange (e.g., due to reaction heat), or in dense gas–particle flows with strong interphase friction or change of the particle volume fraction, even in the absence of chemical reactions (Mačak et al., 2021). The finite speed of sound plays a critical role in certain chemical reactions, particularly in fast processes such as combustion. The ratio between the acoustic propagation time and the chemical reaction time, known as the acoustic Damköhler number (Da), can substantially influence the reaction field (Stöhr et al., 2013). Speed of sound becomes significant when Da is on the order of unity or greater. In such regimes, as observed in vortex–flame interactions, a distinct shift in the heat release pattern occurs once the Damköhler number falls below a critical value of approximately 4 (Ahn and Yu, 2012). Moreover, combustion can generate strong pressure waves, which can lead to self-excited oscillations (Kitano et al., 2013). It has also been reported that the characteristics of pressure waves, such as propagation speed and attenuation, change depending on the fluidization state (Bi, 2007), and conversely, pressure waves can influence fluidization patterns, including bubble formation (Li et al., 2003; Coppens et al., 2002). This highlights the need for simulation tools capable of modeling large-scale reactors while accounting for the intricate coupling between gas and particle dynamics, density changes by chemical reaction, and the propagation of acoustic waves.

Two primary approaches exist for simulating such gas–solid systems: continuum models and discrete models. The Two-Fluid Model (TFM), which treats both the fluid and particle phases as interpenetrating continua, is computationally efficient, making it suitable for large-scale simulations. It has been applied to the simulation of methanation in fluidized beds by researchers such as Li and Yang (Li and Yang, 2019) and Liu and Hinrichsen (Liu and Hinrichsen, 2014). However, the averaging approach inherent to TFM is fundamentally limited in its ability to capture discrete, particle-scale phenomena. In particular, variations in individual particle properties such as volume or density changes induced by chemical reactions are smoothed out through the continuum averaging process. The Discrete Element Method (DEM) (Cundall and Strack, 1979) coupled with Computational Fluid Dynamics (CFD) resolves these particle-scale physics and property changes. This highlights the need for computationally efficient frameworks that leverage the particle-level resolution of DEM to enable the simulation of large-scale reactive systems. However, the choice of the gas solver in a DEM–CFD framework (Tsuji et al., 1993) presents a trade-off between computational cost and physical accuracy. Numerous studies have employed compressible DEM–CFD for reactive flows. Explicit compressible solvers, often used for phenomena such as detonation (Price et al., 2016) or iron reduction (Lan et al., 2024), can resolve acoustic waves. However, they face challenges with computational cost due to the acoustic CFL condition, which limits the time step size. Conversely, pressure-based solvers such as the Semi-Implicit Method for Pressure Linked Equations (SIMPLE) (Patankar, 2018) or the PIMPLE method, which is a combination of SIMPLE and Pressure Implicit with Splitting Operators (PISO), for reactive flows such as biomass gasification (Wang and Shen, 2022) and coal combustion (Huang et al., 2022). While these solvers can handle fully compressible flows and potentially exceed the acoustic CFL limit, their iterative nature for coupling pressure and velocity fields results in a high computational cost, rendering them prohibitive for simulations involving a large number of particles over long durations.

To improve computational efficiency, fractional-step methods are often used as they separate the velocity and pressure calculations, avoiding costly inner iterations. Capecelatro and Desjardins (2013) developed a DEM–CFD framework for reactive flows using a fractional-step method based on the work of Pierce and Moin (2004). While this method is highly efficient, it is based on a formulation that results in pressure waves propagating at an infinite speed. This makes it unsuitable for cases where finite-speed acoustic effects are important. Addressing this, Moureau et al. (2007) developed a fractional-step method for weakly-compressible flows that correctly captures the finite speed of sound. Their method has been successfully applied to methane combustion, but their work did not include a discrete particle phase (Moureau et al., 2011). Following this, Kitano et al. (2013) applied this semi-implicit compressible method to a direct numerical simulation (DNS) of spray combustion, coupling it with a global reaction model to investigate the interaction between pressure perturbations and combustion.

This study bridges the aforementioned gaps by developing and validating a novel DEM–CFD framework for low-Mach number flows. This framework combines the particle-scale accuracy of the DEM with a highly efficient, weakly-compressible fractional-step method proposed by Moureau et al. (2007). Compared to fully compressible methods, this approach is significantly efficient for low-Mach number flows. It decouples the time step from the acoustic CFL constraint and simultaneously avoids ill-conditioning issues that become problematic in fully compressible solvers as the Mach number approaches zero. This provides key flexibility: computational cost can be prioritized by using large time steps (acoustic CFL $> 1$), or acoustic waves can be accurately resolved by adhering to the CFL limit (acoustic CFL $\leq 1$). This paper details the governing equations, the volume averaging technique, and the numerical method. The framework's capabilities are then demonstrated through a series of validation cases. To focus on the fluid–particle dynamics and acoustic aspects of the framework, the cases presented in this study are non-reactive. These include: pressure drop in a fixed bed, particle dynamics in a fluidized bed, and speed of sound measurements in various gases.

## 2. Governing equations

This section details the governing equations used to describe the gas and solid phases in the dense gas–solid multiphase flows under investigation. First, the fundamental point-wise governing equations for the gas phase are presented. These equations are then spatially averaged using the methodology proposed by Anderson and Jackson (1967) to derive the macroscopic equations suitable for multiphase flow simulations. Subsequently, the governing equations for the discrete solid phase, based on the Discrete Element Method (DEM) (Cundall and Strack, 1979), are described, along with the models for interphase coupling.

### 2.1. Gas phase governing equations

#### 2.1.1. Governing equations

At the microscopic level, within the interstitial spaces between particles, the gas phase is assumed to behave as a continuum. This study employs a one-fluid, multi-chemical species approach, in which the gas, although composed of multiple species, is treated as a single mixture for the conservation of mass, momentum, and energy. These equations for the mixture form the basis for deriving the volume averaged equations.

The instantaneous, local conservation of mass for a mixture gas is given by:

$$\frac{\partial \rho_f}{\partial t} + \nabla \cdot (\rho_f \boldsymbol{u}_f) = 0, \tag{1}$$

where $\rho_f$ is the gas density, $\boldsymbol{u}_f$ is the gas velocity vector and $t$ is the time.

The conservation of momentum is expressed as:

$$\frac{\partial}{\partial t}(\rho_f \boldsymbol{u}_f) + \nabla \cdot (\rho_f \boldsymbol{u}_f \otimes \boldsymbol{u}_f) = -\nabla p + \nabla \cdot \boldsymbol{\tau} + \rho_f \mathbf{g}, \tag{2}$$

where $p$ is the pressure, $\boldsymbol{\tau}$ is the viscous stress tensor, and $\mathbf{g}$ is the gravitational acceleration.

The energy equation, in terms of specific enthalpy $h$, is:

$$\frac{\partial}{\partial t}(\rho_f h) + \nabla \cdot (\rho_f h \boldsymbol{u}_f) = \frac{\partial p}{\partial t} + \boldsymbol{u}_f \cdot \nabla p + \nabla \cdot (k \nabla T) + \boldsymbol{\tau} : \nabla \boldsymbol{u}_f, \tag{3}$$

where $k$ is the thermal conductivity and $T$ is the temperature. The specific enthalpy $h$ for an ideal gas is related to temperature by:

$$h = \int_{T_0}^{T} C_p dT + h_0(T_0), \tag{4}$$

where $C_p$ is the specific heat at constant pressure, $T_0$ is a reference temperature and $h_0$ is a reference enthalpy.

For a multi-chemical species gas, the conservation of mass fraction $y_i$ for chemical species $i$ is:

$$\frac{\partial(\rho_f y_i)}{\partial t} + \nabla \cdot (\rho_f \boldsymbol{u}_f y_i) = \nabla \cdot (D_i \nabla y_i), \tag{5}$$

where $D_i$ is the mass diffusivity of chemical species $i$.

The equation of state for an ideal gas mixture is:

$$p = \rho_f R T, \tag{6}$$

where $R$ is the specific gas constant for the mixture. The speed of sound $c$ for an ideal gas, assuming isentropic conditions, is defined as:

$$c = \sqrt{\left(\frac{\partial p}{\partial \rho_f}\right)_s} = \sqrt{\gamma R T}, \tag{7}$$

where $\gamma$ is the ratio of specific heats ($C_p/C_v$), $C_v$ is the specific heat at constant volume.

For the fractional-step method which will appear in Section 3, it is necessary to decouple the direct influence of pressure from the evolution of enthalpy. Therefore, the energy conservation equation is reformulated. By applying the definition of enthalpy, the equation of state, and the definition of the speed of sound, the explicit pressure evolution terms ($\partial p/\partial t$ and $\boldsymbol{u}_f \cdot \nabla p$) can be replaced by terms involving the speed of sound. The detailed derivation of this reformulation is provided in Appendix A. This yields the following pressure-term-free form of the energy equation.

$$\begin{aligned}\frac{\partial}{\partial t}(\rho_f h) + \nabla \cdot (\rho_f h \boldsymbol{u}_f) = &- c^2 \rho_f \nabla \cdot \boldsymbol{u}_f + \gamma \nabla \cdot (k \nabla T) \\ &+ \gamma \boldsymbol{\tau} : \nabla \boldsymbol{u}_f - (\gamma - 1)\rho_f \boldsymbol{u}_f \cdot \nabla h.\end{aligned} \tag{8}$$

Conversely, by combining Eqs. (3) and (8), the enthalpy evolution terms can be eliminated to yield enthalpy-term-free form of the energy equation, also known as the pressure equation:

$$\begin{aligned}\frac{\partial p}{\partial t} + \boldsymbol{u}_f \cdot \nabla p = &- c^2 \rho_f \nabla \cdot \boldsymbol{u}_f + (\gamma - 1)\nabla \cdot (k \nabla T) \\ &+ (\gamma - 1)\boldsymbol{\tau} : \nabla \boldsymbol{u}_f - (\gamma - 1)\rho_f \boldsymbol{u}_f \cdot \nabla h.\end{aligned} \tag{9}$$

#### 2.1.2. Volume averaged governing equations

To make the simulation of dense gas–solid flows computationally tractable, Eqs. (1)–(5) are volume averaged. This work employs the volume averaging technique by Anderson and Jackson (1967), which utilizes a weighting function $g_w(r)$ to define local averaged quantities. The local void fraction $\varepsilon_f(\boldsymbol{x}, t)$ is defined as:

$$\varepsilon_f(\boldsymbol{x}, t) = \int_{\mathcal{V}_f(t)} g_w(|\boldsymbol{x} - \boldsymbol{y}|) dV_y, \tag{10}$$

where the integration is over the domain $\mathcal{V}_f(t)$ occupied by the gas at time $t$.

For any gas quantity $a(\boldsymbol{x}, t)$, its phase volume average $\overline{a}(\boldsymbol{x}, t)$ is defined as:

$$\varepsilon_f \overline{a}(\boldsymbol{x}, t) = \int_{\mathcal{V}_f(t)} a(\boldsymbol{y}, t) g_w(|\boldsymbol{x} - \boldsymbol{y}|) dV_y, \tag{11}$$

The density-weighted phase volume average $\tilde{a}(\boldsymbol{x}, t)$ is defined as:

$$\varepsilon_f \overline{\rho_f} \tilde{a}(\boldsymbol{x}, t) = \int_{\mathcal{V}_f(t)} \rho_f(\boldsymbol{y}, t) a(\boldsymbol{y}, t) g_w(|\boldsymbol{x} - \boldsymbol{y}|) dV_y, \tag{12}$$

where $\overline{\rho_f}$ in Eq. (12) is the phase volume averaged gas density defined according to Eq. (11). Any gas quantity $a$ can be split into the volume averaged and residual component $a = \overline{a} + a'$ or $a = \tilde{a} + a''$. Consequently, $\tilde{\boldsymbol{u}}_f$, $\tilde{h}$, $\tilde{T}$, and $\tilde{y}_i$ represent density-weighted phase volume average quantities, while $\overline{p}$ and $\overline{\boldsymbol{\tau}}$ are phase volume average quantities. By applying the averaging technique (Eqs. (10)–(12)) to the governing equations (Eqs. (1), (2), (5), (8), (9)), we obtain the set of volume averaged equations are as follows.

The averaged continuity equation:

$$\frac{\partial(\varepsilon_f \overline{\rho_f})}{\partial t} + \nabla \cdot (\varepsilon_f \overline{\rho_f} \tilde{\boldsymbol{u}}_f) = S_\rho. \tag{13}$$

The averaged momentum equation:

$$\frac{\partial(\varepsilon_f \overline{\rho_f} \tilde{\boldsymbol{u}}_f)}{\partial t} + \nabla \cdot (\varepsilon_f \overline{\rho_f} \tilde{\boldsymbol{u}}_f \otimes \tilde{\boldsymbol{u}}_f) = -\varepsilon_f \nabla \overline{p} + \nabla \cdot (\varepsilon_f (\overline{\boldsymbol{\tau}} - \boldsymbol{R}_u)) + \varepsilon_f \overline{\rho_f} \mathbf{g} + \boldsymbol{S}_{pu} - \boldsymbol{F}^{inter}. \tag{14}$$

In this equation, the interphase momentum transfer is captured by the gas–particle interaction force $\boldsymbol{F}^{inter}$.

The averaged pressure-term-free form of the energy equation:

$$\begin{aligned}\frac{\partial(\varepsilon_f \overline{\rho_f} \tilde{h})}{\partial t} + \nabla \cdot (\varepsilon_f \overline{\rho_f} \tilde{\boldsymbol{u}}_f \tilde{h}) = &- \varepsilon_f \overline{\rho_f} \overline{c^2} \nabla \cdot \tilde{\boldsymbol{u}}_f + \gamma \nabla \cdot (\varepsilon_f k \nabla \tilde{T}) + \gamma \varepsilon_f \overline{\boldsymbol{\tau}} : \nabla \tilde{\boldsymbol{u}}_f \\ &- (\gamma - 1)\varepsilon_f \overline{\rho_f} \tilde{\boldsymbol{u}}_f \cdot \nabla \tilde{h} - \nabla \cdot \boldsymbol{R}_h + S_{\rho h} \\ &- R_{c \nabla u} - \gamma S_{k \nabla \tilde{T}} + \gamma R_{t \nabla u} - (\gamma - 1) R_{u \nabla h}.\end{aligned} \tag{15}$$

The averaged pressure equation:

$$\begin{aligned}\frac{\partial(\varepsilon_f \overline{p})}{\partial t} + \varepsilon_f \tilde{\boldsymbol{u}}_f \cdot \nabla \overline{p} = &- \varepsilon_f \overline{c^2 \rho_f} \nabla \cdot \tilde{\boldsymbol{u}}_f + (\gamma - 1) \nabla \cdot (\varepsilon_f \overline{k \nabla \tilde{T}}) \\ &+ (\gamma - 1)\varepsilon_f \overline{\boldsymbol{\tau}} : \nabla \tilde{\boldsymbol{u}}_f - (\gamma - 1)\varepsilon_f \overline{\rho_f} \tilde{\boldsymbol{u}}_f \cdot \nabla \tilde{h} \\ &- S_{up} - (\gamma - 1) S_{k \nabla \tilde{T}} - R_{c \nabla u} - R_{u \nabla p} \\ &+ (\gamma - 1) R_{t \nabla u} - \gamma R_{u \nabla h}.\end{aligned} \tag{16}$$

The averaged mass fraction conservation equation for species $i$:

$$\frac{\partial(\varepsilon_f \overline{\rho_f}\tilde{y}_i)}{\partial t} + \nabla\cdot(\varepsilon_f \overline{\rho_f}\tilde{\boldsymbol{u}}_f\tilde{y}_i) = \nabla\cdot(\varepsilon_f D_i \nabla\tilde{y}_i) - \nabla\cdot\boldsymbol{R}_{y_i} + S_{\rho y_i} - S_{D\nabla\tilde{y}_i}. \tag{17}$$

In these equations, the various source terms, denoted by $S$ (e.g., $S_\rho$, $S_{up}$), account for the exchange of mass, momentum, and energy at particle surfaces. The terms denoted by $R$ (e.g., $\boldsymbol{R}_u$, $\boldsymbol{R}_h$) are unclosed residual terms that arise from the averaging process, representing the effects of sub-grid scale phenomena.

The system is closed with the equation of state and the definition for the speed of sound using averaged quantities:

$$\overline{p} = \overline{\rho_f} R\tilde{T}, \tag{18}$$

$$\tilde{c} = \sqrt{\gamma R\tilde{T}}. \tag{19}$$

It is also noted that the residual terms arising from the averaging process are neglected in these expressions.

Previous studies have reported that structure and response of the particles can influence the speed of sound, taking these effects account is complex (Rudinger, 1980; Roy et al., 1990). The model presented in Eq. (19) adopts a simplified assumption where pressure waves do not propagate through the particles and the particle volume does not affect the acoustic properties of the gas. The validity of this approach and a more detailed discussions are provided in Section 5.

### 2.2. Solid phase governing equations (DEM)

The motion of individual solid particles is tracked using the Discrete Element Method (DEM), originally proposed by Cundall and Strack (1979). This method accounts for particle–particle and particle–wall interactions through contact force models.

The translational motion of Particle $i$ with mass $m_i$ and position vector $\boldsymbol{x}_i$ is governed by Newton's second law:

$$m_i \frac{d^2\boldsymbol{x}_i}{dt^2} = \sum_j \boldsymbol{f}_{C,ij} + \boldsymbol{f}_{D,i} + \boldsymbol{f}_{B,i} + m_i\mathbf{g}, \tag{20}$$

where $\boldsymbol{f}_{C,ij}$ and $\boldsymbol{f}_{D,i}$ are the contact force exerted by Particle $j$ (or the walls) and the fluid drag force acting on Particle $i$. $\boldsymbol{f}_{B,i}$ is the buoyancy force defined as $\boldsymbol{f}_{B,i} = -\nabla p V_{p,i}$ where $V_{p,i}$ is the particle volume.

The rotational motion of Particle $i$ with moment of inertia $I_i$ and angular velocity $\boldsymbol{\omega}_i$ is given by:

$$I_i \frac{d\boldsymbol{\omega}_i}{dt} = \sum_j \boldsymbol{M}_{ij}, \tag{21}$$

where $\boldsymbol{M}_{ij}$ is the torque generated by the tangential component of the contact force $\boldsymbol{f}_{C,ij}$. The moment of inertia for a spherical particle of radius $r_i$ is $I_i = 2/5 m_i r_i^2$.

Contact forces $\boldsymbol{f}_{C,ij}$ are modeled using a linear spring–dashpot system. The normal contact force $\boldsymbol{f}_{Cn,ij}$ is given by:

$$\boldsymbol{f}_{Cn,ij} = (-k_n\delta_n - \eta_n \boldsymbol{u}_{n,ij}\cdot\boldsymbol{n}_{ij})\boldsymbol{n}_{ij}, \tag{22}$$

where $k_n$ is the normal spring stiffness, $\delta_n$ is the normal overlap, $\boldsymbol{u}_{n,ij}$ is the normal component of the relative velocity at the contact point, and $\boldsymbol{n}_{ij}$ is the unit normal vector. The normal damping coefficient $\eta_n$ is determined from the coefficient of normal restitution $e_p$ (Tsuji et al., 1992):

$$\eta_n = -\frac{2\ln e_p}{\sqrt{\pi^2 + (\ln e_p)^2}}\sqrt{m k_n}. \tag{23}$$

The tangential contact force $\boldsymbol{f}_{Ct,ij}$ is modeled with a spring and dashpot:

$$\boldsymbol{f}_{Ct,ij} = -\min(|k_t\boldsymbol{\delta}_t + \eta_t \boldsymbol{u}_{s,ij}|, \mu_f|\boldsymbol{f}_{Cn,ij}|)\boldsymbol{t}_{ij}, \tag{24}$$

where $k_t$, $\boldsymbol{\delta}_t$, $\eta_t$, $\boldsymbol{u}_{s,ij}$, $\mu_f$, and $\boldsymbol{t}_{ij}$ are the tangential stiffness, displacement, damping, relative surface velocity, friction coefficient, and unit tangential vector, respectively.

The fluid force $\boldsymbol{f}_{D,i}$ acting on each Particle $i$ is composed of a drag force and a force due to the macroscopic pressure gradient of the fluid:

$$\boldsymbol{f}_{D,i} = \left\{\frac{\beta}{1-\varepsilon_f}(\tilde{\boldsymbol{u}}_f - \boldsymbol{u}_i)\right\} V_{p,i}, \tag{25}$$

where $\boldsymbol{u}_i$ is the velocity of Particle $i$, and $\beta$ is the interphase momentum transfer coefficient. In the present study, we only consider low-Mach number flows as test cases where the effects of compressibility on the drag coefficient are considered negligible, and employs Gidaspow model (Gidaspow, 1994) for $\beta$ based on the Ergun equation (Ergun, 1952) for dense regions ($\varepsilon_f \le 0.8$) and the Wen and Yu correlation (Wen, 1966) for dilute regions ($\varepsilon_f > 0.8$). The model is expressed as:

$$\beta = \begin{cases} \frac{\mu_f(1-\varepsilon_f)}{d_p^2\varepsilon_f}\{150(1-\varepsilon_f) + 1.75 Re_p\} & (\varepsilon_f \le 0.8) \\ \frac{3}{4}C_D\frac{\mu_f(1-\varepsilon_f)}{d_p^2}\varepsilon_f^{-2.7} Re_p & (\varepsilon_f > 0.8), \end{cases} \tag{26}$$

where $\mu_f$ is the fluid viscosity, $d_p$ is the particle diameter, and $Re_p$ is the particle Reynolds number based on the average particle velocity $\hat{\boldsymbol{u}}_p$:

$$Re_p = \frac{\overline{\rho_f}\varepsilon_f d_p|\tilde{\boldsymbol{u}}_f - \hat{\boldsymbol{u}}_p|}{\mu_f}. \tag{27}$$

The drag coefficient $C_D$ for a single sphere is given by the Schiller and Naumann correlation (Schiller, 1933):

$$C_D = \begin{cases} 24(1 + 0.15 Re_p^{0.687})/Re_p & (Re_p \le 1000) \\ 0.43 & (Re_p > 1000). \end{cases} \tag{28}$$

### 2.3. Interphase coupling terms

The gas and solid phases are coupled primarily through the interfacial momentum transfer. The term $\boldsymbol{F}^{inter}$ in the gas momentum Eq. (14) represents the force exerted by the particles on the gas. By Newton's third law, this force is equal in magnitude and opposite in direction to the sum of all fluid dynamic forces, $\boldsymbol{f}_{D,i}$, acting on the particles within a control volume. The interaction force is calculated as:

$$\boldsymbol{F}^{inter} = \frac{1}{V_{cell}}\sum_i \left\{\frac{\beta}{1-\varepsilon_f}(\tilde{\boldsymbol{u}}_f - \boldsymbol{u}_i)V_{p,i}\right\}, \tag{29}$$

where the sum is over particles in the fluid cell of volume $V_{cell}$. The other source terms, such as $S_\rho$, $\boldsymbol{S}_{\rho u}$, $S_{\rho h}$, and $S_{\rho y_i}$, account for mass, momentum, and energy exchanged at the particle surfaces, which are critical when considering chemical reactions or phase changes.

## 3. Numerical method

This section outlines the numerical method for solving the volume averaged gas phase equations. The method is based on a fractional-step method for weakly-compressible flows (Moureau et al., 2007).

### 3.1. Overall computational procedure

The gas solver is based on the weakly-compressible approach of Moureau et al. (2007), which is designed to efficiently simulate low-Mach number flows while retaining acoustic effects. The core of the method is a fractional-step method that decouples the advective–diffusive phenomena from the acoustic phenomena. This characteristic splitting is based on the decomposition of the eigenvalues of the 1D compressible Navier–Stokes equations (Moureau et al., 2007):

$$\begin{pmatrix} u+c \\ u-c \\ u \end{pmatrix} = \begin{pmatrix} u \\ u \\ u \end{pmatrix} + \begin{pmatrix} c \\ -c \\ 0 \end{pmatrix} \tag{30}$$

Here, the eigenvalues $u + c$ and $u - c$ represent the acoustic waves, while $u$ represents advection. The splitting mathematically separates the governing equations into a pure advection operator and a pure acoustic operator. This allows the physical phenomena to be solved in

two main sub-steps: a predictor step that handles the advection and diffusion, followed by a corrector step that implicitly handles the acoustic wave propagation. This semi-implicit strategy improves computational efficiency by avoiding the need for costly inner iterations.

The particles and gas phase are weakly coupled:

1. **Particle Motion Calculation (DEM):**
   Particle positions and velocities for the next time step $n+1$ are computed based on the forces from the current time step. This yields the updated void fraction $\varepsilon_f^{n+1}$ and interphase source terms (e.g., $\boldsymbol{F}^{inter}$, $S_\rho$).
2. **Gas Dynamics Calculation (Fractional-Step Method):**
   The gas governing equations are then solved for the next time step using the updated information from the DEM step. This calculation consists of prediction and correction sub-steps.

### 3.1.1. Prediction step

In the prediction step, predicted values for the gas variables ($\overline{\rho_f}^*$, $\tilde{\boldsymbol{u}}_f^*$, $\tilde{h}^*$, $\tilde{y}_i^*$) are computed by solving the advection–diffusion forms of the conservation equations shown in Eqs. (31)–(34). In these equations, all terms without a temporal superscript are evaluated using known quantities from the previous time step, $n$. These prediction equations omit the pressure gradient term in the momentum equation and terms related to the speed of sound in the energy equation. It should be noted that the advection operator in Eqs. (31)–(34) is split into two terms, following the characteristic splitting approach of Moureau et al. (2007). As will be shown in the correction step, the third terms in the left-hand side are associated with the terms involving the speed of sound (Eq. (41)), thereby allowing for a separation between advective and acoustic phenomena.

$$\frac{\varepsilon_f^{n+1}\overline{\rho_f}^* - \varepsilon_f^{n+1}\overline{\rho_f}^n}{\Delta t} + \nabla\cdot(\varepsilon_f^{n+1}\overline{\rho_f}^n\tilde{\boldsymbol{u}}_f^n) - \varepsilon_f^{n+1}\overline{\rho_f}^n\nabla\cdot\tilde{\boldsymbol{u}}_f^n = S_\rho, \tag{31}$$

$$\begin{aligned}\frac{\varepsilon_f^{n+1}\overline{\rho_f}^*\tilde{\boldsymbol{u}}_f^* - \varepsilon_f^{n+1}\overline{\rho_f}^n\tilde{\boldsymbol{u}}_f^n}{\Delta t} &+ \nabla\cdot(\varepsilon_f^{n+1}\overline{\rho_f}^n\tilde{\boldsymbol{u}}_f^n\otimes\tilde{\boldsymbol{u}}_f^n) - \varepsilon_f^{n+1}\overline{\rho_f}^n\tilde{\boldsymbol{u}}_f^n\nabla\cdot\tilde{\boldsymbol{u}}_f^n \\ &= \varepsilon_f^{n+1}\nabla\cdot(\overline{\boldsymbol{\tau}} - \boldsymbol{R}_u) + \varepsilon_f^{n+1}\overline{\rho_f}^n\mathbf{g} + \boldsymbol{S}_{\rho u} - \boldsymbol{F}^{inter},\end{aligned} \tag{32}$$

$$\begin{aligned}\frac{\varepsilon_f^{n+1}\overline{\rho_f}^*\tilde{h}^* - \varepsilon_f^{n+1}\overline{\rho_f}^n\tilde{h}^n}{\Delta t} &+ \nabla\cdot(\varepsilon_f^{n+1}\overline{\rho_f}^n\tilde{\boldsymbol{u}}_f^n\tilde{h}^n) - \varepsilon_f^{n+1}\overline{\rho_f}^n\tilde{h}^n\nabla\cdot\tilde{\boldsymbol{u}}_f^n \\ &= \gamma\nabla\cdot(\varepsilon_f^{n+1}k\nabla\tilde{T}^n) + \gamma\varepsilon_f^{n+1}\overline{\boldsymbol{\tau}} : \nabla\tilde{\boldsymbol{u}}_f^n \\ &- (\gamma-1)\varepsilon_f^{n+1}\overline{\rho_f}^n\tilde{\boldsymbol{u}}_f^n\cdot\nabla\tilde{h}^n - \nabla\cdot\boldsymbol{R}_h + S_{\rho h} \\ &- R_{c\nabla u} - \gamma S_{k\nabla\tilde{T}} + \gamma R_{t\nabla u} - (\gamma-1)R_{u\nabla h},\end{aligned} \tag{33}$$

$$\begin{aligned}\frac{\varepsilon_f^{n+1}\overline{\rho_f}^*\tilde{y}_i^* - \varepsilon_f^{n+1}\overline{\rho_f}^n\tilde{y}_i^n}{\Delta t} &+ \nabla\cdot(\varepsilon_f^{n+1}\overline{\rho_f}^n\tilde{\boldsymbol{u}}_f^n\tilde{y}_i^n) - \varepsilon_f^{n+1}\overline{\rho_f}^n\tilde{y}_i^n\nabla\cdot\tilde{\boldsymbol{u}}_f^n \\ &= \nabla\cdot(\varepsilon_f^{n+1}D_i\nabla\tilde{y}_i^n) + S_{\rho y_i} - S_{D\nabla y_i}.\end{aligned} \tag{34}$$

Subsequently, $\tilde{T}^*$ is determined from $\tilde{h}^*$ and $\tilde{y}_i^*$. The predicted pressure $\overline{p}^*$ is then calculated from the equation of state (18) using $\overline{\rho_f}^*$ and $\tilde{T}^*$. Finally, the predicted speed of sound $\tilde{c}^*$ is also determined from its definition (19) using these predicted properties.

### 3.1.2. Pressure correction step

The pressure correction step adjusts the predicted gas variables to satisfy the full conservation Eqs. (13)–(15), (17) by accounting for the acoustic phenomena that were omitted from the prediction step. Consequently, the following correction equations explicitly involve terms related to pressure and the speed of sound. It is a key feature of this non-iterative approach that these equations are linearized by evaluating all coefficients using the known predicted (*) state. This linearization allows the updated variables at the $n+1$ step to be solved without inner iterations, as follows:

$$\frac{\varepsilon_f^{n+1}\overline{\rho_f}^{n+1} - \varepsilon_f^{n+1}\overline{\rho_f}^*}{\Delta t} + \varepsilon_f^{n+1}\overline{\rho_f}^*\nabla\cdot\tilde{\boldsymbol{u}}_f^* = 0, \tag{35}$$

$$\frac{\varepsilon_f^{n+1}\overline{\rho_f}^{n+1}\tilde{\boldsymbol{u}}_f^{n+1} - \varepsilon_f^{n+1}\overline{\rho_f}^*\tilde{\boldsymbol{u}}_f^*}{\Delta t} + \varepsilon_f^{n+1}\overline{\rho_f}^*\tilde{\boldsymbol{u}}_f^*\nabla\cdot\tilde{\boldsymbol{u}}_f^* = -\frac{\varepsilon_f^{n+1}}{2}\nabla(\overline{p}^n + \overline{p}^{n+1}), \tag{36}$$

$$\frac{\varepsilon_f^{n+1}\overline{\rho_f}^{n+1}\tilde{h}^{n+1} - \varepsilon_f^{n+1}\overline{\rho_f}^*\tilde{h}^*}{\Delta t} + \varepsilon_f^{n+1}\overline{\rho_f}^*\tilde{h}^*\nabla\cdot\tilde{\boldsymbol{u}}_f^* = -\varepsilon_f^{n+1}\tilde{c}^{*2}\overline{\rho_f}^*\nabla\cdot\tilde{\boldsymbol{u}}_f^*, \tag{37}$$

$$\frac{\varepsilon_f^{n+1}\overline{\rho_f}^{n+1}\tilde{y}_i^{n+1} - \varepsilon_f^{n+1}\overline{\rho_f}^*\tilde{y}_i^*}{\Delta t} + \varepsilon_f^{n+1}\overline{\rho_f}^*\tilde{y}_i^*\nabla\cdot\tilde{\boldsymbol{u}}_f^* = 0. \tag{38}$$

The corresponding correction for pressure, Eq. (39), is derived from the full pressure equation, Eq. (16). Since all terms other than the acoustic term (involving the speed of sound, $c$) have already been accounted for in the prediction step, the correction step simplifies to the following relationship:

$$\frac{\varepsilon_f^{n+1}\overline{p}^{n+1} - \varepsilon_f^{n+1}\overline{p}^*}{\Delta t} = -\varepsilon_f^{n+1}\tilde{c}^{*2}\overline{\rho_f}^*\nabla\cdot\tilde{\boldsymbol{u}}_f^*. \tag{39}$$

The pressure at time step $n+1$ is related to the predicted pressure $\overline{p}^*$ and a pressure correction term $\delta\overline{p}$ as:

$$\delta\overline{p} = \overline{p}^{n+1} - \overline{p}^*. \tag{40}$$

Substituting this definition of $\overline{p}^{n+1}$ into Eq. (39), we get:

$$\frac{\varepsilon_f^{n+1}\delta\overline{p}}{\Delta t} = -\varepsilon_f^{n+1}\tilde{c}^{*2}\overline{\rho_f}^*\nabla\cdot\tilde{\boldsymbol{u}}_f^*. \tag{41}$$

Using this relationship in Eq. (41), the following equations are derived from Eqs. (35)–(38).

$$\frac{\varepsilon_f^{n+1}\overline{\rho_f}^{n+1} - \varepsilon_f^{n+1}\overline{\rho_f}^*}{\Delta t} - \frac{1}{\Delta t}\frac{\varepsilon_f^{n+1}\delta\overline{p}}{\tilde{c}^{*2}} = 0, \tag{42}$$

$$\frac{\varepsilon_f^{n+1}\overline{\rho_f}^{n+1}\tilde{\boldsymbol{u}}_f^{n+1} - \varepsilon_f^{n+1}\overline{\rho_f}^*\tilde{\boldsymbol{u}}_f^*}{\Delta t} - \frac{\varepsilon_f^{n+1}\tilde{\boldsymbol{u}}_f^*}{\tilde{c}^{*2}}\frac{\delta\overline{p}}{\Delta t} = -\frac{\varepsilon_f^{n+1}}{2}\nabla(\overline{p}^n + \overline{p}^* + \delta\overline{p}), \tag{43}$$

$$\frac{\varepsilon_f^{n+1}\overline{\rho_f}^{n+1}\tilde{h}^{n+1} - \varepsilon_f^{n+1}\overline{\rho_f}^*\tilde{h}^*}{\Delta t} - \frac{(\tilde{h}^* + \tilde{c}^{*2})}{\tilde{c}^{*2}}\frac{\varepsilon_f^{n+1}\delta\overline{p}}{\Delta t} = 0, \tag{44}$$

$$\frac{\varepsilon_f^{n+1}\overline{\rho_f}^{n+1}\tilde{y}_i^{n+1} - \varepsilon_f^{n+1}\overline{\rho_f}^*\tilde{y}_i^*}{\Delta t} - \frac{\tilde{y}_i^*}{\tilde{c}^{*2}}\frac{\varepsilon_f^{n+1}\delta\overline{p}}{\Delta t} = 0. \tag{45}$$

Taking the divergence of Eq. (43) and using the continuity equation to remove the unknown term leads to the Helmholtz equation for $\delta\overline{p}$, the detailed derivation is provided in Appendix B.

$$\begin{aligned}\nabla\cdot\nabla\delta\overline{p} + \frac{\nabla\varepsilon_f^{n+1}}{\varepsilon_f^{n+1}}\cdot\nabla\delta\overline{p} - \frac{2}{\varepsilon_f^{n+1}}\nabla\cdot\left(\frac{\varepsilon_f^{n+1}\tilde{\boldsymbol{u}}_f^*}{\tilde{c}^{*2}}\frac{\delta\overline{p}}{\Delta t}\right) - \frac{4}{\tilde{c}^{*2}\Delta t^2}\delta\overline{p} \\ = -\nabla\cdot\nabla(\overline{p}^n + \overline{p}^*) - \frac{\nabla\varepsilon_f^{n+1}}{\varepsilon_f^{n+1}}\cdot\nabla(\overline{p}^n + \overline{p}^*) \\ + \frac{4}{\varepsilon_f^{n+1}\Delta t}\left[\frac{\varepsilon_f^{n+1}\overline{\rho_f}^* - \varepsilon_f^n\overline{\rho_f}^n}{\Delta t} + \nabla\cdot\left(\frac{\varepsilon_f^{n+1}\overline{\rho_f}^*\tilde{\boldsymbol{u}}_f^* + \varepsilon_f^n\overline{\rho_f}^n\tilde{\boldsymbol{u}}_f^n}{2}\right) - S_\rho\right]\end{aligned} \tag{46}$$

It is noted, unlike the elliptic Poisson equation found in incompressible solvers (which yields an infinite speed of sound), this Helmholtz equation is hyperbolic in nature. This property enables the framework to correctly capture the propagation of acoustic waves at a finite speed.

### 3.1.3. Correction step

Once the pressure correction $\delta\overline{p}$ is obtained by solving the Helmholtz Eq. (46), the corrected gas variables at time step $n+1$ are determined. The now-known values of $\delta\overline{p}$ and the predicted speed of sound $\tilde{c}^*$ are substituted into the pressure correction Eqs. (42)–(45). These equations are then solved for the corrected variables: $\overline{p}^{n+1}, \overline{\rho_f}^{n+1}, \tilde{\boldsymbol{u}}_f^{n+1}, \tilde{h}^{n+1}, \tilde{y}_i^{n+1}$. Finally, $\tilde{T}^{n+1}$ is updated using $\tilde{h}^{n+1}$ and $\tilde{y}_i^{n+1}$.

## 4. Discretization and implementation details

The numerical framework was implemented in an in-house code, DEr (Discrete Element solver for dense reactive gas–solid flows), using a Cartesian coordinate system with a uniform grid for the fluid cells for each directions. Initially, all spatial derivatives were discretized using a second-order central difference scheme; however, numerical instabilities were observed. To enhance stability, the advection terms were discretized using an upwind scheme. Although a second-order upwind scheme was also tested, a first-order upwind scheme was ultimately adopted in this study to prioritize robustness. For the time integration, the gas advection–diffusion equations were solved using an explicit third-order Runge–Kutta method, while the particle motion in the DEM was advanced using the first-order Euler–Cromer method. Fluid quantities required for particle force calculations were taken from the volume-averaged values of the cell containing the particle center, although interpolation from surrounding cells is a possible refinement. The Helmholtz equation for the pressure correction was solved using the Bi-Conjugate Gradient Stabilized (Bi-CGSTAB) method (Van der Vorst, 1992). The unclosed source ($S$) and residual ($R$) terms arising from the volume averaging (Eqs. (13)–(17)) were neglected in this study for simplicity. The physical properties of the chemical species, such as molecular weight and specific heat, were obtained as a function of temperature and pressure using CHEMKIN-formatted libraries (Kee et al., 1986, 1989).

## 5. Validation

### 5.1. General setup and numerical approaches

This section presents the validation of the newly proposed numerical framework through three fundamental test cases. Unless otherwise specified for a particular case, the gas was considered to be dry air (23% oxygen, 77% nitrogen by mass), with an initial temperature of 300 K, initial pressure of $1 \times 10^5$ Pa, and zero initial velocity. Particle beds were prepared by allowing particles to settle randomly from an elevated position, after which excess particles were removed to achieve the desired initial bed height. For the gas phase, boundary conditions were set as follows. Gas was introduced from the bottom boundary at a temperature of 300 K, with the velocity specified as the superficial velocity. The top boundary was an atmospheric (1 atm). All other boundaries were treated as slip walls, with zero-gradient conditions applied to the other gas variables. While the semi-implicit fluid solver is designed to be stable at large time steps (i.e., for acoustic CFL > 1), the complex interactions introduced by the coupled particle phase necessitated a smaller time step to ensure overall stability. Accordingly, a fixed time step of $1 \times 10^{-5}$ s or $5 \times 10^{-5}$ s was used for the simulations presented in the following section.

### 5.2. Pressure drop

#### 5.2.1. Computational conditions

To validate the gas–particle interaction model, the pressure drop across the particle bed and the minimum fluidization velocity were evaluated. The computational setup (Fig. 1) and parameters (Table 1) were adapted from the work of Van Buijtenen et al. (2012). While the $x-y$ dimensions of the domain and the particle parameters are identical to their simulation, the particle bed height and the $z$-dimension were set to form an initially cubic particle bed. To isolate gas–particle interactions from wall effects on fluidization, the particle–wall friction coefficient was set to zero for this test case. The superficial gas velocity at the inlet was increased gradually with a small acceleration (0.1 m/s$^2$).

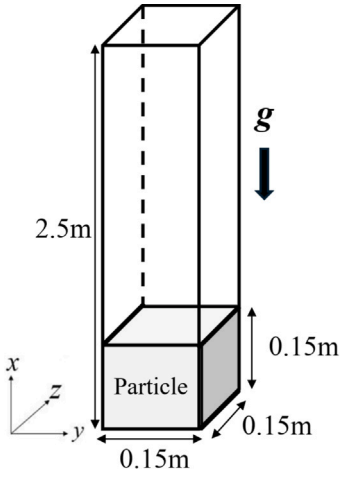


**Fig. 1.** Computational domain for the pressure drop test.

**Table 1**
Simulation parameters for pressure drop test.

| | | |
|---|---|---|
| Bed | | |
| Height ($L_x$) | [m] | 2.5 |
| Width ($L_y$) | [m] | 0.15 |
| Depth ($L_z$) | [m] | 0.15 |
| Particle | | |
| Sphericity | [–] | 1 |
| Number | [–] | 154,206 |
| Diameter | [m] | $3.0 \times 10^{-3}$ |
| Density | [kg/m$^3$] | 2505 |
| Normal spring constant | [N/m] | 10,000 |
| Poisson's ratio | [–] | 0.25 |
| Coefficient of restitution(normal) | [–] | 0.97 |
| Coefficient of friction (particle–particle) | [–] | 0.1 |
| Coefficient of friction (particle–wall) | [–] | 0 |
| Gas | | |
| Cells in $x$-direction | [–] | 250 |
| Cells in $y$-direction | [–] | 20 |
| Cells in $z$-direction | [–] | 20 |
| Cell size in $x$-direction ($\Delta x$) | [m] | $10 \times 10^{-3}$ |
| Cell size in $y$-direction ($\Delta y$) | [m] | $7.5 \times 10^{-3}$ |
| Cell size in $z$-direction ($\Delta z$) | [m] | $7.5 \times 10^{-3}$ |
| Initial void fraction | [–] | 0.34 |
| Time step | [s] | $1 \times 10^{-5}$ |

#### 5.2.2. Results and discussion

The computed pressure drop versus superficial fluid velocity is compared with the Ergun equation (Ergun, 1952) in Fig. 2. The predicted minimum fluidization velocity ($u_{mf} \approx 1.15$ m/s) also matched well with the theoretical value (1.13 m/s), and the pressure drop in the fluidized state (2290 Pa) was close to the theoretical particle weight per unit area (2380 Pa).

The slight discrepancy observed in the fixed-bed region can be attributed to the different treatment of the void fraction. While the Ergun equation is based on a single, bulk-averaged void fraction, the simulation resolves the gas–particle interaction forces according to the local void fraction in each computational cell. This contrast between the homogeneous assumption of the theory and the spatially resolved heterogeneity in the simulation is the likely source of the minor deviation. These results show good agreement, validating the basic momentum exchange model.

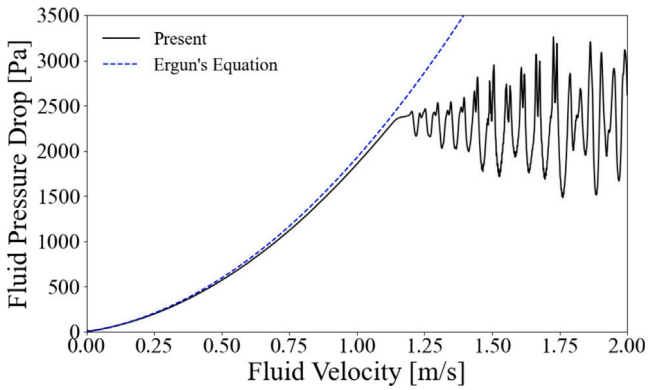


**Fig. 2.** Pressure drop versus superficial fluid velocity. The simulation results are compared with the Ergun equation.

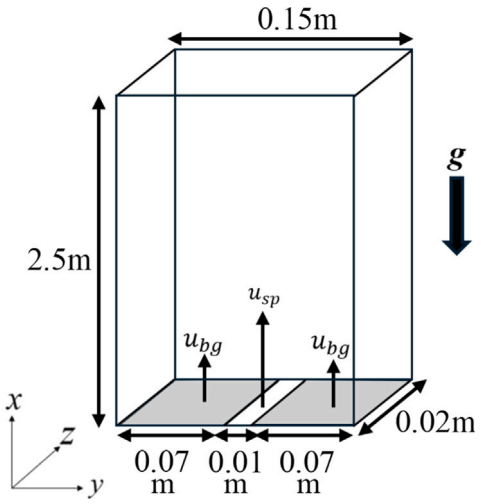


**Fig. 3.** Computational domain for the fluidization state test.

### 5.3. Fluidization state

#### 5.3.1. Computational conditions

Particle dynamics in a fluidized state were validated against the experimental and numerical work of Van Buijtenen et al. (2012). A central jet ($u_{sp}$ = 37.25 m/s) and background flow ($u_{bg}$ = 4.15 m/s) were introduced as per the experiment (Fig. 3). The parameters listed in Table 2 were adopted from their numerical study (Van Buijtenen et al., 2012); notably, this includes the reference values for the coefficient of restitution and the friction coefficient, which are subjects of later discussion.

#### 5.3.2. General flow pattern and particle velocities

The simulation revealed a dynamic flow field, with max variations in gas pressure and density of approximately 1.2% and 1.1%, respectively. Fig. 4 shows instantaneous snapshots of key gas properties at $t$ = 10.0 s. The void fraction distribution (Fig. 4(a)) indicates that the particles are in a well-fluidized state. The gas pressure field, shown in Fig. 4(b), varies in accordance with the local particle distribution. The gas density distribution (Fig. 4(c)) is observed to be nearly identical to the pressure distribution. This is a reasonable result, as the simulation is nearly isothermal, and for an ideal gas, density is approximately proportional to pressure under such conditions.

Fig. 5 compares the simulated time-averaged vertical particle velocities, measured at a height of 0.1 m along the centerline in the depth direction and averaged over 20 s, with experimental data (PEPT, PIV) from Van Buijtenen et al. (2012). General trends and symmetry are reproduced, but discrepancies exist near the center and walls.

**Table 2**
Simulation parameters for fluidization state test.

| | | |
|---|---|---|
| **Bed** | | |
| Height ($L_x$) | [m] | 2.5 |
| Width ($L_y$) | [m] | 0.15 |
| Depth ($L_z$) | [m] | 0.020 |
| **Particle** | | |
| Sphericity | [–] | 1 |
| Number | [–] | 12,479 |
| Diameter | [m] | $3.0 \times 10^{-3}$ |
| Density | [kg/m$^3$] | 2505 |
| Normal spring constant | [N/m] | 10,000 |
| Poisson's ratio | [–] | 0.25 |
| Coefficient of restitution(normal) | [–] | 0.97 |
| Coefficient of friction (particle–particle) | [–] | 0.1 |
| Coefficient of friction (particle–wall) | [–] | 0.3 |
| Initial bed height | [m] | 0.1 |
| **Gas** | | |
| Cells in $x$-direction | [–] | 250 |
| Cells in $y$-direction | [–] | 30 |
| Cells in $z$-direction | [–] | 2 |
| Cell size in $x$-direction ($\Delta x$) | [m] | $10 \times 10^{-3}$ |
| Cell size in $y$-direction ($\Delta y$) | [m] | $5 \times 10^{-3}$ |
| Cell size in $z$-direction ($\Delta z$) | [m] | $10 \times 10^{-3}$ |
| Time step | [s] | $1 \times 10^{-5}$ |

The discrepancies observed prompted a sensitivity analysis on DEM contact parameters. As shown in Figs. 6 and 7, the particle velocity profiles are highly sensitive to the coefficient of restitution ($e_p$) and friction ($\mu_p$), underscoring the importance of accurate parameter calibration for quantitative predictions.

### 5.4. Speed of sound measurement

#### 5.4.1. Computational conditions

This study validates the framework's ability to handle weakly-compressible effects by simulating the propagation of a pressure wave through a particle bed (Fig. 8) for various gases (Dry Air, $CO_2$, $H_2$) at different gas temperatures. The parameters used are given in Table 3. Through parameter sensitivity analysis of speed of sound measurements, it was confirmed that results are independent of the parameters listed in Table 3 when sufficient spatial resolution is available (see Appendix C for details). Method for determining the speed of sound from simulation data are also described in Appendix C.

#### 5.4.2. Results and discussion

Fig. 9 compares the measured speeds with the theoretical values for a pure ideal gas, given by $c = \sqrt{\gamma RT/M}$, where $M$ is the molecular weight of the gas mixture. Excellent agreement was found, confirming the framework's ability to accurately handle finite speed of sound propagation and species-dependent properties. As stated in Section 2, the speed of sound here is calculated using Eq. (19). This formulation assumes that pressure waves do not propagate through the particles and that the particle volume does not affect the acoustic properties of the interstitial gas. Therefore, under this specific formulation, it is a valid result that the pressure wave propagates unaffected by the presence of the solid phase.

To validate the framework's ability to capture the influence of the particle phase on wave propagation, an alternative model for the speed of sound was tested in a second set of simulations for dry air at 300 K. This test was based on the "frozen flow" (Rudinger, 1980), which assumes that flow changes occur so rapidly that the particles cannot follow, leaving their velocity and temperature unaffected by the acoustic wave. The speed of sound in such a medium is referred to as the "frozen speed of sound". Similar to the formulation in Eq. (19),

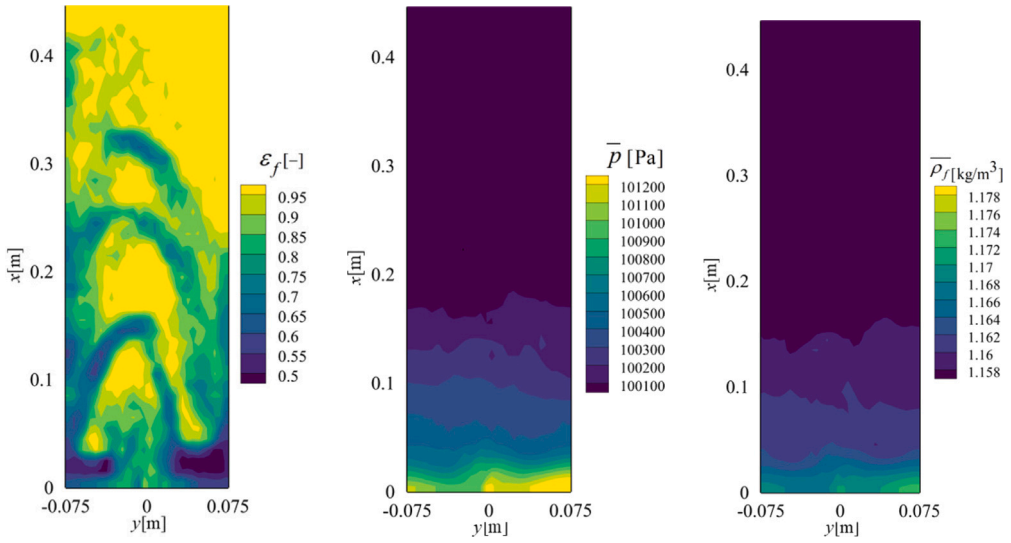


(a) Void fraction. (b) Gas pressure. (c) Gas density.

**Fig. 4.** Instantaneous snapshots of gas properties at $t = 10.0$ s.

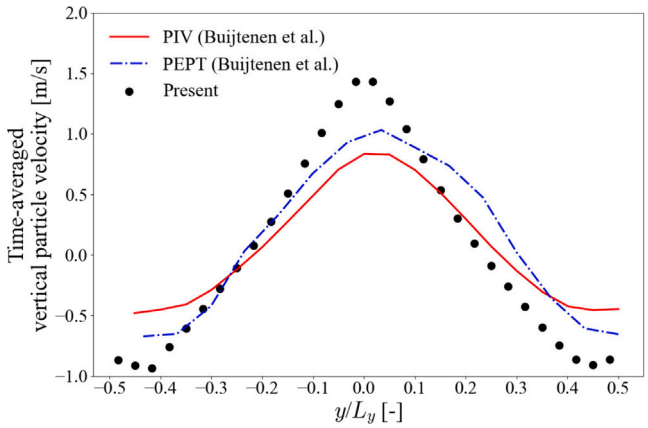


**Fig. 5.** Time-averaged vertical particle velocities on the centerline at a height of 0.1 m, compared with experimental data from Van Buijtenen et al. (2012).

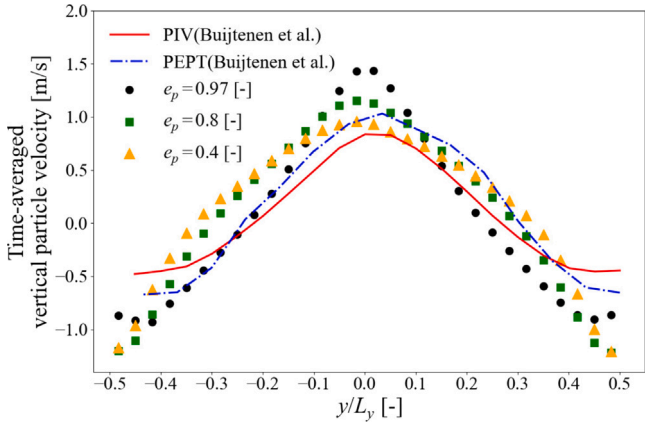


**Fig. 6.** Effect of coefficient of restitution ($e_p$) on time-averaged vertical particle velocities.

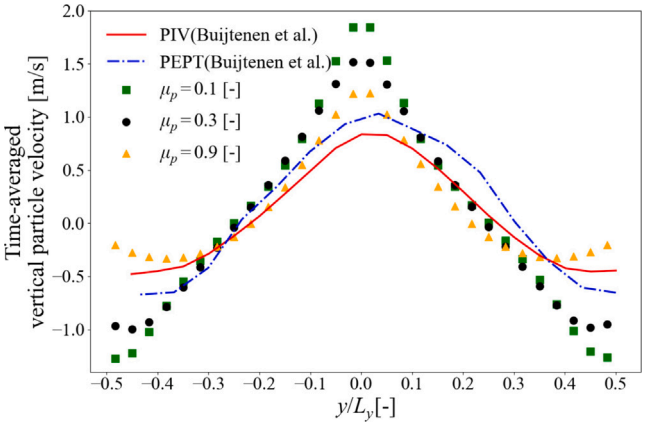


**Fig. 7.** Effect of friction coefficient ($\mu_p$) on time-averaged vertical particle velocities.

this model assumes that pressure waves do not propagate through the particles; however, it does account for the influence that the particle volume has on wave propagation. The frozen speed of sound ($c_f$) can be expressed as (Rudinger, 1980):

$$c_f = \sqrt{\frac{\gamma R\tilde{T}}{\varepsilon_f}}. \tag{47}$$

For this validation, the particle bed was held fixed under adiabatic conditions. To vary the bulk void fraction, the same initial packing structure was used, and the particle diameter was systematically reduced.

The results of this second study are shown in Fig. 10. Overall, the simulation results demonstrate the flamework's ability to handle the dependency of the frozen speed of sound on the void fraction. At lower void fractions, the measured speed of sound is notably higher than the single-phase gas value and closely approaches the theoretical line for the frozen speed of sound. As the void fraction increases, the

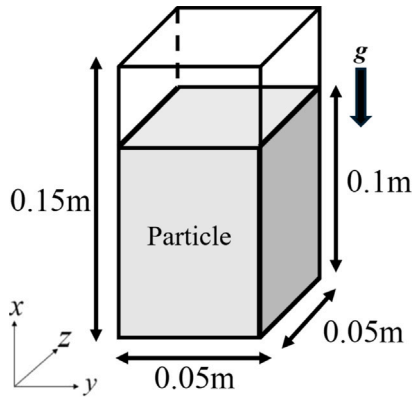


**Fig. 8.** Computational domain for the speed of sound measurement.

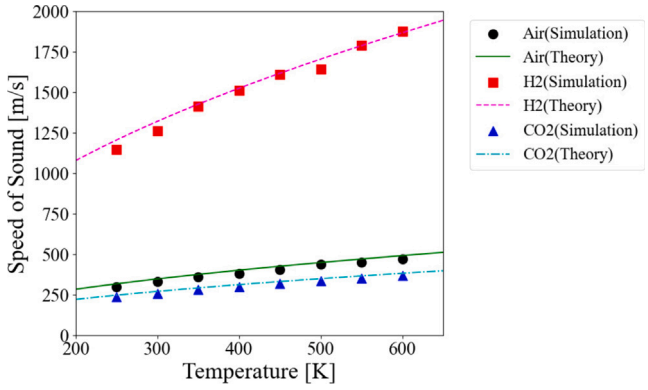


**Fig. 9.** Speed of sound in various gases at different temperatures, compared with theoretical values (lines).

measured speed deviates from the frozen speed theory and asymptotically approaches the theoretical value for the pure ideal gas. The increasing error from the frozen speed theory at higher void fractions is likely attributable to the difference in how the speed of sound is determined. The theoretical line is calculated using the bulk void fraction for the entire domain. In contrast, the simulation calculates the speed of sound locally at each point, based on the actual void fraction in that location. This is although to create a discrepancy between the constant theoretical speed and the spatially varying local speed within the simulation, which may in turn lead to the diffusion of the pressure wave front.

These results demonstrate that the speed of sound within the simulation can be intentionally altered by changing its definition. This underscores the flexibility of the framework. However, it also highlights that the physically appropriate model for the speed of sound depends on factors such as the fluidization state and the response of the particles to pressure fluctuations. As other studies have reported, another models exist for the speed of sound in well-fluidized states where the particles are able to follow the motion of the gas (Roy et al., 1990). It is crucial to select a suitable model based on the specific physical conditions being investigated.

## 6. Conclusion

In this study, an efficient numerical framework for simulating dense, reactive gas–solid flows was developed and validated. The methodology combines the Discrete Element Method (DEM) for resolving the particle phase with a volume averaged gas equations solved by a weakly-compressible fractional-step method. This approach was designed to bridge the gap between computationally prohibitive, fully compressible DEM–CFD solvers and faster methods that neglect important acoustic phenomena.

A series of validation cases confirmed the framework's capabilities. Simulations of pressure drop in a fixed bed and particle dynamics in a spout-fluidized bed demonstrated that the framework accurately captures fundamental gas–particle momentum exchange and complex hydrodynamic behaviors. These tests also highlighted the critical role of particle contact parameters (restitution and friction coefficients), underscoring the need for their careful calibration to achieve quantitative accuracy. Furthermore, a key study on acoustic wave propagation validated the framework's central feature: its ability to reproduce the correct finite speed of sound for various gases at different temperatures, using species properties derived from CHEMKIN libraries. The flexibility of the framework was further highlighted in a second study, where the framework also successfully reproduced an alternative theoretical frozen speed of sound for the two-phase mixture. Together, these

**Table 3**
Simulation parameters for speed of sound measurement.

| | | |
|---|---|---|
| Bed | | |
| Height($L_x$) | [m] | 0.15 |
| Width($L_y$) | [m] | 0.05 |
| Depth($L_z$) | [m] | 0.05 |
| Particle | | |
| Sphericity | [–] | 1 |
| Number | [–] | 280,784 |
| Diameter | [m] | $1.0 \times 10^{-3}$ |
| Density | [kg/m$^3$] | 1036 |
| Normal spring constant | [N/m] | 800 |
| Poisson's ratio | [–] | 0.25 |
| Coefficient of restitution(normal) | [–] | 0.9 |
| Coefficient of friction | [–] | 0.3 |
| Initial bed height | [m] | 0.1 |
| Gas | | |
| Chemical species | [–] | Dry Air/CO2/H2 |
| Temperature | [K] | 250, 300, …, 600 |
| Cells in $x$-direction | [–] | 60 |
| Cells in $y$-direction | [–] | 20 |
| Cells in $z$-direction | [–] | 20 |
| Cell size in $x$-direction($\Delta x$) | [m] | $2.5 \times 10^{-3}$ |
| Cell size in $y$-direction($\Delta y$) | [m] | $2.5 \times 10^{-3}$ |
| Cell size in $z$-direction($\Delta z$) | [m] | $2.5 \times 10^{-3}$ |
| Time step | [s] | $5 \times 10^{-5}$ |

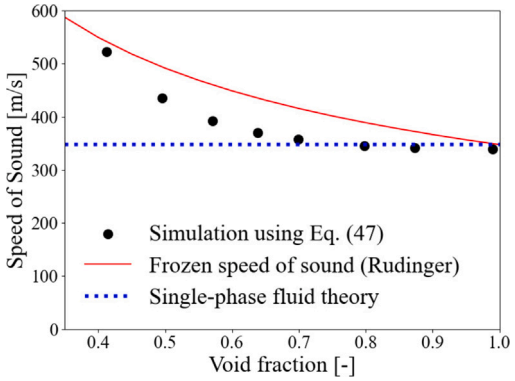


**Fig. 10.** Speed of sound predicted using Eq. (47) as a function of bulk void fraction, compared with the theoretical frozen speed of sound (Rudinger, 1980) (solid red line) and the single-phase gas theory (dotted blue line). (For interpretation of the references to color in this figure legend, the reader is referred to the web version of this article.)

acoustic studies demonstrate that the framework can capture different physical regimes of sound propagation, confirming that the physically appropriate model for the speed of sound depends on factors such as the response of the particles to the acoustic waves.

In conclusion, this work establishes a robust, efficient, and physically comprehensive numerical tool for the study of reactive gas–solid multiphase systems. By successfully integrating a non-iterative fluid solver capable of resolving acoustic wave propagation with a discrete particle model, this framework is now well-positioned for application to its motivating problem: the large-scale simulation fluidized bed reactors especially methanation. Future work will focus on implementing reaction kinetics to investigate the crucial link between reaction-induced density changes and fluidization efficiency.

## CRediT authorship contribution statement

**Yuki Yakata:** Writing – original draft, Visualization, Validation, Software, Investigation. **Kimiaki Washino:** Writing – review & editing, Supervision, Software, Methodology. **Masaya Muto:** Writing – review & editing, Software, Resources. **Ryoichi Kurose:** Writing – review & editing, Supervision, Conceptualization. **Takuya Tsuji:** Writing – review & editing, Supervision, Software, Project administration, Investigation, Conceptualization.

## Declaration of competing interest

The authors declare that they have no known competing financial interests or personal relationships that could have appeared to influence the work reported in this paper.

## Acknowledgments

The authors are grateful to Hiroaki Watanabe for his insightful comments and continuous support throughout this work.

## Appendix A. Derivation of the pressure-term-free energy equation

This appendix details the reformulation of the energy equation to eliminate the terms including pressure, resulting in Eq. (8). The derivation is based on the thermodynamic relations for an ideal gas.

From Mayer's relation, we have:

$$R = C_p - C_v. \tag{A.1}$$

From the ideal gas law, Eq. (6), and the definition of the speed of sound, Eq. (7), pressure can be expressed as:

$$p = \rho_f \frac{c^2}{\gamma}. \tag{A.2}$$

Using the definition of specific heat at constant pressure, $C_p = (\partial h/\partial T)_p$, a relationship between the differentials of enthalpy, pressure, and density can be derived. By expressing the total differential of temperature $\delta T$ in terms of $\delta p$ and $\delta \rho_f$ and substituting it into the enthalpy definition, we obtain:

$$\rho_f \delta h = \frac{\gamma}{\gamma - 1}\left(\delta p - \frac{c^2}{\gamma}\delta\rho_f\right). \tag{A.3}$$

Rearranging Eq. (A.3) to solve for the pressure differential gives a key thermodynamic relation:

$$\delta p = \frac{\gamma - 1}{\gamma}\rho_f \delta h + \frac{c^2}{\gamma}\delta\rho_f. \tag{A.4}$$

Taking the partial derivative of Eq. (A.4) with respect to time and applying the product rule to the enthalpy term yields the expression for the time derivative of pressure:

$$\begin{aligned}\frac{\partial p}{\partial t} &= \frac{\gamma - 1}{\gamma}\rho_f \frac{\partial h}{\partial t} + \frac{c^2}{\gamma}\frac{\partial \rho_f}{\partial t} \\ &= \frac{\gamma - 1}{\gamma}\left(\frac{\partial(\rho_f h)}{\partial t} - h\frac{\partial \rho_f}{\partial t}\right) + \frac{c^2}{\gamma}\frac{\partial \rho_f}{\partial t}.\end{aligned} \tag{A.5}$$

Finally, the pressure terms in the original enthalpy-based energy equation, Eq. (3), are eliminated. This is achieved by substituting the expression for $\partial p/\partial t$ from Eq. (A.5) and the expression for $p$ from Eq. (A.2) into the $\boldsymbol{u}_f \cdot \nabla p$ term. After simplification using the continuity equation, Eq. (1), and substantial algebraic rearrangement, we obtain the final pressure-term-free form of the energy equation:

$$\begin{aligned}\frac{\partial}{\partial t}(\rho_f h) + \nabla\cdot(\rho_f h \boldsymbol{u}_f) = &- c^2\rho_f \nabla\cdot\boldsymbol{u}_f + \gamma\nabla\cdot(k\nabla T) \\ &+ \gamma\boldsymbol{\tau} : \nabla\boldsymbol{u}_f - (\gamma - 1)\rho_f \boldsymbol{u}_f \cdot \nabla h.\end{aligned} \tag{A.6}$$

## Appendix B. Derivation of the Helmholtz equation for pressure correction

This appendix details the derivation of the Helmholtz equation for the pressure correction, Eq. (46). The derivation is based on the following set of correction-step equations.

The momentum correction is given by Eq. (43). Taking the divergence of this equation yields:

$$\begin{aligned}&\nabla\cdot\left(\frac{\varepsilon_f^{n+1}\overline{\rho_f}^{n+1}\tilde{\boldsymbol{u}}_f^{n+1} - \varepsilon_f^{n+1}\overline{\rho_f}^{*}\tilde{\boldsymbol{u}}_f^{*}}{\Delta t}\right) - \nabla\cdot\left(\frac{\varepsilon_f^{n+1}\tilde{\boldsymbol{u}}_f^{*}}{\tilde{c}^{*2}}\frac{\delta\overline{p}}{\Delta t}\right) \\ &= -\frac{1}{2}\nabla\cdot\left(\varepsilon_f^{n+1}\nabla(\overline{p}^n + \overline{p}^{*} + \delta\overline{p})\right).\end{aligned} \tag{B.1}$$

To eliminate the unknown velocity term, $\nabla\cdot(\varepsilon_f\overline{\rho_f}\tilde{\boldsymbol{u}}_f)^{n+1}$, the second-order accurate time discretization of the continuity equation is used:

$$\frac{\varepsilon_f^{n+1}\overline{\rho_f}^{n+1} - \varepsilon_f^{n}\overline{\rho_f}^{n}}{\Delta t} + \nabla\cdot\left(\frac{\varepsilon_f^{n+1}\overline{\rho_f}^{n+1}\tilde{\boldsymbol{u}}_f^{n+1} + \varepsilon_f^{n}\overline{\rho_f}^{n}\tilde{\boldsymbol{u}}_f^{n}}{2}\right) = S_\rho. \tag{B.2}$$

Additionally, the density at the new time step, $\overline{\rho_f}^{n+1}$, is substituted using the density correction relationship from Eq. (42):

$$\varepsilon_f^{n+1}\overline{\rho_f}^{n+1} = \varepsilon_f^{n+1}\overline{\rho_f}^{*} + \frac{\varepsilon_f^{n+1}\delta\overline{p}}{\tilde{c}^{*2}}. \tag{B.3}$$

By substituting these relationships into Eq. (B.1) and rearranging all terms involving the unknown $\delta\overline{p}$ to the left-hand side, we obtain the final Helmholtz equation:

$$\begin{aligned}&\nabla\cdot\nabla\delta\overline{p} + \frac{\nabla\varepsilon_f^{n+1}}{\varepsilon_f^{n+1}}\cdot\nabla\delta\overline{p} - \frac{2}{\varepsilon_f^{n+1}}\nabla\cdot\left(\frac{\varepsilon_f^{n+1}\tilde{\boldsymbol{u}}_f^{*}}{\tilde{c}^{*2}}\frac{\delta\overline{p}}{\Delta t}\right) - \frac{4}{\tilde{c}^{*2}\Delta t^2}\delta\overline{p} \\ &= -\nabla\cdot\nabla(\overline{p}^n + \overline{p}^{*}) - \frac{\nabla\varepsilon_f^{n+1}}{\varepsilon_f^{n+1}}\cdot\nabla(\overline{p}^n + \overline{p}^{*}) \\ &\quad + \frac{4}{\varepsilon_f^{n+1}\Delta t}\left[\frac{\varepsilon_f^{n+1}\overline{\rho_f}^{*} - \varepsilon_f^{n}\overline{\rho_f}^{n}}{\Delta t} + \nabla\cdot\left(\frac{\varepsilon_f^{n+1}\overline{\rho_f}^{*}\tilde{\boldsymbol{u}}_f^{*} + \varepsilon_f^{n}\overline{\rho_f}^{n}\tilde{\boldsymbol{u}}_f^{n}}{2}\right) - S_\rho\right]\end{aligned} \tag{B.4}$$

## Appendix C. Method for speed of sound measurement and sensitivity analysis

This appendix details the specific method used to measure the speed of sound presented in Section 5.4 and the sensitivity analyses performed to confirm the robustness of these measurements.

### C.1. Method of measurement

The speed of sound was defined as the propagation speed of a pressure wave through the particle bed. The system was initially at $1 \times 10^5$ Pa. A planar pressure wave was generated by instantaneously increasing the pressure at the bottom boundary ($x = 0$ m) to $2 \times 10^5$ Pa at $t = 0$ s. To track the wave front's position over time, the gas pressure was monitored. Specifically, the pressure was averaged in the horizontal ($y - z$) plane at each height ($x$ coordinate). The wave front position was measured as the height at which the gauge pressure

first exceeded 1 Pa. Sensitivity tests using different pressure thresholds showed slight differences in the detected wave front position at each time step, however, these variations did not significantly affect the resulting speed of sound; therefore, the 1 Pa threshold was adopted. The speed of sound was then determined from the slope of a linear least-squares fit applied to the position–time data of the wave front in the height range from $x = 0$ m to $x = 0.1$ m.

### C.2. Parameters sensitivity analyses

The tested sound speed models depend primarily on gas properties and, for Eq. (47), void fraction (addressed in Fig. 10). Since particles were fixed in these simulations, DEM mechanical parameters (Table 3) do not influence wave propagation through the interstitial gas.

Domain boundary effects were minimized. Planar wave generation at the bottom boundary negates horizontal dependence. The speed measurement was performed within the region of the particle bed (0 m to 0.1 m), ensuring wave front analysis occurred before any reflections from the top boundary could interfere. Therefore, the results are considered independent of the domain size.

A grid size independence study was conducted specifically for the streamwise $x$-direction cell size ($\Delta x$), as this is the primary direction of wave propagation. Using the setup for Dry Air at 300 K with the speed of sound definition (Eq. (19)), three grid resolutions were tested:

1. Fine Grid: $\Delta x = 1.25 \times 10^{-3}$ m (Half the baseline size in Table 3)
2. Baseline Grid: $\Delta x = 2.5 \times 10^{-3}$ m (Original size from Table 3)
3. Coarse Grid: $\Delta x = 5.0 \times 10^{-3}$ m (Double the baseline size in Table 3)

The measured speed of sound for each case were 329 m/s, 329 m/s, and 411 m/s, respectively. The convergence of the results between the fine and baseline grids confirms that the baseline grid resolution ($\Delta x = 2.5 \times 10^{-3}$ m) provides sufficient spatial resolution to capture the pressure wave propagation.

## Data availability

Data will be made available on request.

## References


Ahn, K., Yu, K.H., 2012. Effects of Damköhler number on vortex–flame interaction. Combust. Flame 159 (2), 686–696.

Anderson, T.B., Jackson, R., 1967. Fluid mechanical description of fluidized beds. Equations of motion. Ind. Eng. Chem. Fundam. 6 (4), 527–539.

Bi, H.T., 2007. A critical review of the complex pressure fluctuation phenomenon in gas–solids fluidized beds. Chem. Eng. Sci. 62 (13), 3473–3493.

Capecelatro, J., Desjardins, O., 2013. An Euler–Lagrange strategy for simulating particle-laden flows. J. Comput. Phys. 238, 1–31.

Coppens, M.-O., Regelink, M.A., van den Bleek, C.M., 2002. Pulsation induced transition from chaos to periodically ordered patterns in fluidised beds. In: Proceedings of 4th World Congress on Particle Technology (WCPT), Sydney. pp. 1–8.

Cundall, P.A., Strack, O.D.L., 1979. A discrete numerical model for granular assemblies. Geotechnique 29 (1), 47–65.

Ergun, S., 1952. Fluid flow through packed columns. Chem. Eng. Prog. 48, 89–94.

Gidaspow, D., 1994. Multiphase flow and fluidization: continuum and kinetic theory descriptions.

Huang, C.C., van Oijen, J.A., Deen, N.G., Tang, Y., 2022. Incorporation of flamelets generated manifold method in coarse-grained Euler-Lagrange simulations of pulverized coal combustion. Chem. Eng. Sci. 260, 117838.

Kai, T., Toriyama, K., Nishie, K., Takahashi, T., Nakajima, M., 2006. Effect of volume decrease on fluidization quality of fluidized catalyst beds. AIChE J. 52 (9), 3210–3215.

Kee, R.J., Dixon-Lewis, G., Warnatz, J., Coltrin, M.E., Miller, J.A., 1986. A Fortran computer code package for the evaluation of gas-phase multicomponent transport properties. SAND86-8246, Sandia National Laboratories.

Kee, R.J., Rupley, F.M., Miller, J.A., 1989. CHEMKIN-II: A fortran chemical kinetics package for the analysis of gas-phase chemical kinetics. SAND89-8009B, Sandia National Laboratories.

Kitano, T., Kurose, R., Komori, S., 2013. Effects of internal pressure and inlet velocity disturbances of air and fuel droplets on spray combustion field. J. Therm. Sci. Technol. 8 (1), 269–280.

Lan, B., Xu, J., Lu, S., Liu, Y., Xu, F., Zhao, B., Zou, Z., Zhai, M., Wang, J., 2024. Direct reduction of iron-ore with hydrogen in fluidized beds: A coarse-grained CFD-DEM-IBM study. Powder Technol. 438, 119624.

Li, J., Aranson, I.S., Kwok, W.-K., Tsimring, L.S., 2003. Periodic and disordered structures in a modulated gas-driven granular layer. Phys. Rev. Lett. 90 (13), 134301.

Li, J., Yang, B., 2019. Multi-scale CFD simulations of bubbling fluidized bed methanation process. Chem. Eng. J. 377, 119818.

Liu, Y., Hinrichsen, O., 2014. CFD simulation of hydrodynamics and methanation reactions in a fluidized-bed reactor for the production of synthetic natural gas. Ind. Eng. Chem. Res. 53 (22), 9348–9356.

Mačak, J., Goniva, C., Radl, S., 2021. Regimes of subsonic compressible flow in gas-particle systems. Powder Technol. 394, 44–61.

Moureau, V., Bérat, C., Pitsch, H., 2007. An efficient semi-implicit compressible solver for large-eddy simulations. J. Comput. Phys. 226 (2), 1256–1270.

Moureau, V., Domingo, P., Vervisch, L., 2011. From large-eddy simulation to direct numerical simulation of a lean premixed swirl flame: Filtered laminar flame-pdf modeling. Combust. Flame 158 (7), 1340–1357.

Patankar, S., 2018. Numerical Heat Transfer and Fluid Flow. CRC Press.

Pierce, C.D., Moin, P., 2004. Progress-variable approach for large-eddy simulation of non-premixed turbulent combustion. J. Fluid Mech. 504, 73–97.

Price, M.A., Nguyen, V.-T., Hassan, O., Morgan, K., 2016. An Euler–Lagrange particle approach for modeling fragments accelerated by explosive detonation. Internat. J. Numer. Methods Engrg. 106 (11), 904–926.

Roy, R., Davidson, J.F., Tuponogov, V.G., 1990. The velocity of sound in fluidised beds. Chem. Eng. Sci. 45 (11), 3233–3245.

Rudinger, G., 1980. Fundamentals of Gas Particle Flow, vol. 2, Elsevier.

Schiller, L., 1933. Über die grundlegenden berechnungen bei der schwerkraftaufbereitung. Z. Vereines Dtsch. Inge. 77, 318–321.

Stöhr, M., Arndt, C.M., Meier, W., 2013. Effects of Damköhler number on vortex–flame interaction in a gas turbine model combustor. Proc. Combust. Inst. 34 (2), 3107–3115.

Tsuji, Y., Kawaguchi, T., Tanaka, T., 1993. Discrete particle simulation of two-dimensional fluidized bed. Powder Technol. 77 (1), 79–87.

Tsuji, Y., Tanaka, T., Ishida, T., 1992. Lagrangian numerical simulation of plug flow of cohesionless particles in a horizontal pipe. Powder Technol. 71 (3), 239–250.

Van Buijtenen, M.S., Buist, K., Deen, N.G., Kuipers, J.A.M., Leadbeater, T., Parker, D.J., 2012. Numerical and experimental study on spout elevation in spout-fluidized beds. AIChE J. 58 (8), 2524–2535.

Van der Vorst, H.A., 1992. Bi-CGSTAB: A fast and smoothly converging variant of Bi-CG for the solution of nonsymmetric linear systems. SIAM J. Sci. Stat. Comput. 13 (2), 631–644.

Wang, S., Shen, Y., 2022. Coarse-grained CFD-DEM modelling of dense gas-solid reacting flow. Int. J. Heat Mass Transfer 184, 122302.

Wen, C.Y., 1966. Mechanics of fluidization. In: The Chemical Engineering Progress Symposium Series, vol. 62, pp. 100–111.